

## Observation of electric-dipole transitions in the laser-cooling candidate $\text{Th}^-$ and its application for cooling antiprotons

Rulin Tang,<sup>1,\*</sup> Ran Si,<sup>2,\*</sup> Zejie Fei,<sup>3</sup> Xiaoxi Fu,<sup>1</sup> Yuzhu Lu,<sup>1</sup> Tomas Brage<sup>Ⓞ,4</sup>  
 Hongtao Liu<sup>Ⓞ,3,†</sup>, Chongyang Chen,<sup>2,‡</sup> and Chuangang Ning<sup>Ⓞ,1,5,§</sup>

<sup>1</sup>Department of Physics, State Key Laboratory of Low-Dimensional Quantum Physics, Tsinghua University, Beijing 100084, China

<sup>2</sup>Shanghai EBIT Lab, Key Laboratory of Nuclear Physics and Ion-Beam Application (MOE), Institute of Modern Physics, Department of Nuclear Science and Technology, Fudan University, Shanghai 200433, China

<sup>3</sup>Key Laboratory of Interfacial Physics and Technology, Shanghai Institute of Applied Physics, Chinese Academy of Sciences, Shanghai 201800, China

<sup>4</sup>Division of Mathematical Physics, Department of Physics, Lund University, P.O. Box 118, 221 00 Lund, Sweden

<sup>5</sup>Collaborative Innovation Center of Quantum Matter, Beijing 100084, China



(Received 14 November 2019; revised 25 September 2020; accepted 1 April 2021; published 20 April 2021)

Despite the fact that the laser-cooling method is a well-established technique to obtain ultracold neutral atoms and atomic cations, it has rarely if ever been applied to atomic anions due to the lack of suitable electric-dipole transitions. Efforts of more than a decade have until recently only resulted in  $\text{La}^-$  as a promising anion candidate for laser cooling, but our previous work [Tang *et al.*, *Phys. Rev. Lett.* **123**, 203002 (2019)] showed that  $\text{Th}^-$  is also a potential candidate. Here we report on a combination of experimental and theoretical studies to determine the frequencies and rates, as well as branching ratios, for the relevant transitions in  $\text{Th}^-$ . The resonant frequency of the laser-cooling transition is determined to be  $\nu = 123.455(30)$  THz [ $\lambda = 2428.4(6)$  nm]. The transition rate is calculated as  $A = 1.17 \times 10^4 \text{ s}^{-1}$ . Since the branching fraction to dark states is negligible,  $1.47 \times 10^{-10}$ , this represents an ideal closed cycle in  $\text{Th}^-$  for laser cooling. Furthermore, the zero nuclear spin of  $^{232}\text{Th}$  makes the cooling process possible in a Penning trap, which can be used to confine both antiprotons and  $\text{Th}^-$  ions. The presented ion dynamics simulations show that the laser-cooled  $\text{Th}^-$  anions can effectively cool antiprotons to a temperature around 10 mK.

DOI: [10.1103/PhysRevA.103.042817](https://doi.org/10.1103/PhysRevA.103.042817)

### I. INTRODUCTION

The ability to cool atoms and positive ions to  $\mu\text{K}$  or even lower temperatures via laser-cooling techniques has opened many new and exciting opportunities in atomic and molecular physics. Although laser cooling is a well-established technique for producing ultracold neutral atoms and positive ions, more work needs to be done to achieve this for negative ions. In principle, once we produce ultracold ensembles of a specific anion system, we can use them to sympathetically cool any anions, ranging from elementary particles to molecular anions, which will promote the research of cold plasma [1], ultracold chemistry [2], and fundamental-physics tests [3–8]. Particularly, the laser-cooled anions were proposed to sympathetically cool antiprotons, as a step towards producing ultracold antihydrogen atoms [9]. A challenge in this is that the magnetic potential well is shallow for antihydrogen atoms, and therefore they can only be trapped if they are very cold; in other words, the temperature is less than about 0.5 K. Due to their larger weight, the antiprotons, not the positrons, are the main contributors to the temperature of the produced antihydrogen. Thus, the antiprotons must be as cool as possible

in order to enhance the capture probability. By now, there are three separate methods for cooling antiprotons: sympathetic cooling using electrons [10], adiabatic cooling [11], and evaporative cooling [12]. In the ATRAP, ALPHA, and ASACUSA experiments, antiprotons are confined together with electrons in a cryogenic Penning trap, where the electrons lose energy via the emission of cyclotron radiation in the magnetic field and can be cooled to thermal equilibrium with the cryogenic walls of the trap, reaching a quite low temperature [7,13–15]. In turn the heavier antiprotons transfer kinetic energy to electrons through collisions. With this method, the temperature of the antiprotons and electrons can be cooled to around a few kelvins. In current state of the art experiments, the best result is about 20 antihydrogen atoms trapped from a single mixing sequence of 90 000 antiprotons and 1.6 million positrons [16–18]. In contrast to this, laser-cooled anions can be used to sympathetically cool antiprotons to a much lower temperature, which may eventually strongly enhance the trapping efficiency, leading to the possibility for tests of fundamental symmetries, such as charge-parity-time symmetry in matter-antimatter [19], and the direct measurement of the Earth's gravitational acceleration on antihydrogen [20].

In contrast to neutral atoms and positive ions, which have an infinite number of bound states, negative ions have in most cases only a single bound state. The reason is that in an atomic anion, the excess electron is bound mainly via polarization and correlation effects [21]. The potential

\*These authors contributed equally to this work.

†liuhongtao@sinap.ac.cn

‡chychen@fudan.edu.cn

§ningcg@tsinghua.edu.cn

experienced by this extra electron is shallow and of short range, and therefore it usually does not possess bound excited states [21,22]. There are a few exceptions to this rule, with atomic anions having bound excited states. It is even more rare that these bound states are of opposite parity to the ground state [21,23], opening up the possibility of electric-dipole (E1) bound-bound transitions. Presently there are only three reported E1 observations in atomic anions, namely,  $\text{Os}^-$  [9,23–26],  $\text{Ce}^-$  [27,28], and  $\text{La}^-$  [23,29–31], where only  $\text{La}^-$  is a promising candidate for laser cooling [31]. The frequency and rate of the laser-cooling transition were determined to be  $\nu = 96.592\,713(91)$  THz [30,31] and  $A = 4.90(50) \times 10^4 \text{ s}^{-1}$  [31], respectively. Unfortunately, there are two major obstacles to using  $\text{La}^-$  for cooling: the existence of dark states and the nuclear spin of the most abundant isotope. The dark states involved in the cooling transition cycle  ${}^3F_2^e \leftrightarrow {}^3D_1^o$  lead to populations of metastable states. As an example, during the period of laser cooling an ensemble of  $\text{La}^-$  ions from 100 K to Doppler temperature  $T_D = 0.17 \mu\text{K}$ , roughly 40% of  $\text{La}^-$  will end up in the metastable state  ${}^3F_3^e$  with a lifetime of 132 s [31]. The nuclear spin of  ${}^{139}\text{La}^-$  is  $7/2$ , resulting in a rather complex hyperfine structure, with five levels within the ground state  ${}^3F_2^e$  of  ${}^{139}\text{La}^-$  (with  $F = 11/2, 9/2, 7/2, 5/2, 3/2$ ), three for the excited state  ${}^3D_1^o$  (with  $F = 9/2, 7/2, 5/2$ ), and seven for the metastable state  ${}^3F_3^e$  (with  $F = 13/2, 11/2, 9/2, 7/2, 5/2, 3/2, 1/2$ ). Since several hyperfine levels involved in the cooling cycle are dark states, repumping laser beams are required to close the transition cycle [30]. In addition to  $\text{La}^-$ , the molecular anion  $\text{C}_2^-$  has been proposed as another candidate [5,9,32], but it introduces the challenge to recycle vibrational and rotational branching of the cooling transition [5,32].

In a recent publication, we pointed out that  $\text{Th}^-$  is a potential candidate for laser cooling, based on results from high-resolution photoelectron energy spectroscopy and high-level theoretical calculations [33]. In this work, the electron affinity (EA) of  $\text{Th}^-$  was determined to be  $4901.35(48) \text{ cm}^{-1}$  or  $607.690(60) \text{ meV}$  and the transition candidate for laser cooling was identified as  ${}^4F_{3/2}^e \leftrightarrow {}^2S_{1/2}^o$  with a frequency of 117 THz ( $\lambda = 2.56 \mu\text{m}$ ), and a relatively fast rate of  $A = 1.17 \times 10^4 \text{ s}^{-1}$ . Since the  ${}^{232}\text{Th}$  isotope has zero nuclear spin and therefore no hyperfine structure, it introduces much less potential complication for laser cooling than the earlier candidates discussed above. This advantage is even more emphasized for sympathetically cooling antiprotons via laser-cooled anions. In the ALPHA and AEGIS schemes for producing cold antihydrogen, the decelerated antiprotons are trapped and precooled in a Penning trap [7,8]. The strong magnetic field of a few teslas used to confine antiprotons in these traps introduces a higher complexity in both cases due to the Zeeman effect. However, this is less severe in the relatively simple structure of  $\text{Th}^-$ , for which the ground state  ${}^4F_{3/2}^e$  and the excited state  ${}^2S_{1/2}^o$  only split up into four and two magnetic sublevels, respectively (see Discussion below). This is in sharp contrast to the hyperfine affected system  $\text{La}^-$ , or the molecular  $\text{C}_2^-$ , which both will become very complex in a magnetic field. The laser cooling in a Penning trap is more attractive than in a Paul trap because the precooled antiproton can be transferred and trapped efficiently using the same magnetic field.

In this paper, we report on experimental observation of the bound-bound electrical dipole transitions in  $\text{Th}^-$  from the ground state  ${}^4F_{3/2}^e$  to excited states  ${}^2S_{1/2}^o$ ,  ${}^4F_{5/2}^o$ , and  ${}^4D_{1/2}^o$  using the resonant two-photon detachment method. In this experiment we determined the resonance frequencies and obtained two-photon detachment photoelectron spectra at these frequencies. Based on the previous theoretical calculations, we further extended the search for all possible bound states of  $\text{Th}^-$ . To address to which degree the cooling cycle is closed, all relevant branching ratios of transitions were deduced. In addition to this, we calculated the Zeeman splittings and described the laser-cooling recycle in the magnetic field of the Penning trap. Moreover, to demonstrate the sympathetic cooling effects on antiprotons via laser-cooled  $\text{Th}^-$ , ion dynamics simulations were performed.

## II. EXPERIMENTAL METHOD

The experiment was conducted using our cryogenic slow electron velocity-mapping imaging (cryo-SEVI) spectrometer [34–36], which was described in detail in earlier publications [37] and in Fig. 1. The slow electron velocity-mapping imaging (SEVI) method has a high-energy resolution for low kinetic energy electrons. We have used this method to determine the electron affinities (EAs) of several transition elements [38–40], such as Re [41], Hf [42], and La [43]. In the present experiment,  $\text{Th}^-$  ions were produced by laser sputtering on a pure thorium metal disk. Generated anions lost their kinetic energy via collisions with the buffer gas and were trapped in a radio-frequency (RF) octupole ion trap, mounted on a cryogenically cold head with a controlled temperature in the range 5–300 K. In this experiment, the mixture of 20%  $\text{H}_2$  and 80%  $\text{He}$  was used as the buffer gas, which was delivered by a pulsed valve.  $\text{Th}^-$  anions were stored in the trap for a period of 45 ms, and the temperature was kept at 300 K. Under the experimental conditions, our experimental results showed that all excited  $\text{Th}^-$  decayed to the ground state. The trapped anions were then extracted via pulsed potentials on the end caps of the ion trap and analyzed by a Wiley-McLaren type time of flight (TOF) mass spectrometer [44]. Using a mass gate, we could select  $\text{Th}^-$  anions via a setting of  $m = 232$ . Next, a probing laser beam with an adjustable wavelength intersected the ion beam orthogonally and photodetached  $\text{Th}^-$ . The emitted electrons formed a spherical shell and were projected onto a phosphor screen by the electric field of the velocity-map imaging system [45,46]. Each bright spot fired by a photoelectron on the phosphor screen was captured and its position was recorded by a CCD camera with an event-counting mode. Since the probing laser beam was linearly polarized parallel to the phosphor screen, the distribution of photoelectrons had cylindrical symmetry. Hence, the three-dimensional (3D) photoelectron spherical shell can be reconstructed from the projected two-dimensional (2D) distribution without losing information. We used the maximum-entropy reconstruction method [47] to reconstruct the distribution of photoelectrons. The corresponding binding energy (BE) of the detachment channel was extracted from  $\text{BE} = h\nu - \alpha r^2$ , where  $h\nu$  is the photon energy,  $r$  is the radius of the spherical shell, and  $\alpha$  is a calibration coefficient, which can be determined by varying  $h\nu$ . This imaging mode for

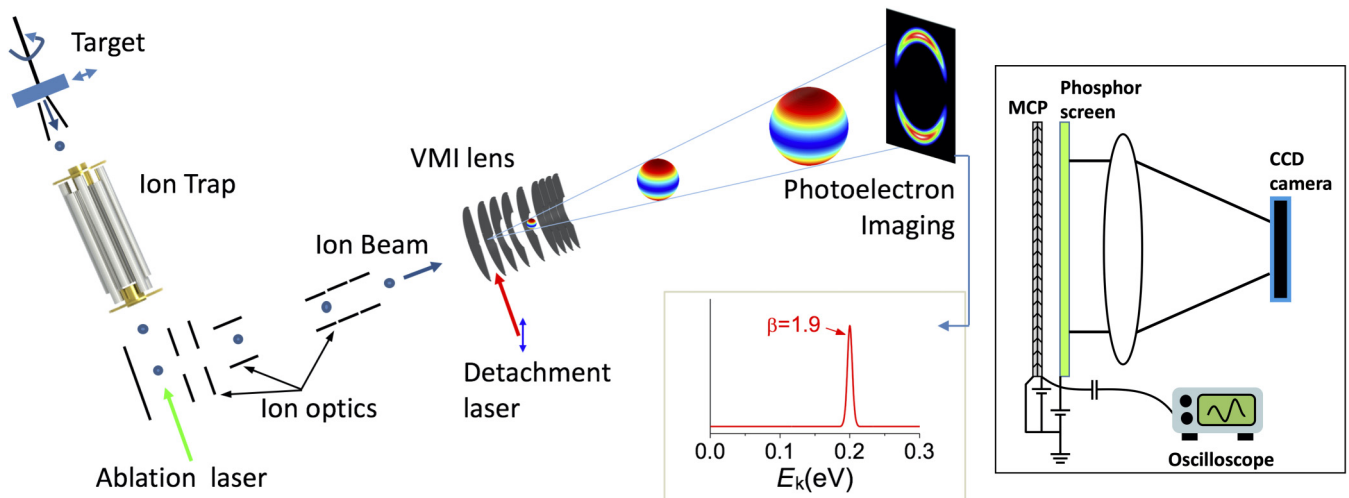


FIG. 1. Schematic view of our cryo-SEVI spectrometer. The Einzel lens before the ion trap, the mass gate, and the ion detector before the VMI lens are not shown. The inset on the right shows the readout of the phosphor screen using a CCD camera or an oscilloscope.

acquiring photoelectron energy spectra was called the SEVI mode. To avoid the interference of  $\text{Th}^-$  anions during the SEVI mode, the high voltage on MCP can be gated on for  $0.8 \mu\text{s}$  only for photoelectrons since our CCD camera used for reading the fluorescence was not fast enough to discriminate photoelectrons from  $\text{Th}^-$  ions.

To observe the E1 transitions in  $\text{Th}^-$ , we have recently updated the imaging system of the spectrometer, making it possible to switch from the standard SEVI mode to the scanning mode. In the scanning mode, the phosphor screen was used as a charged particle detector. A high-speed oscilloscope was connected to the phosphor screen to record both the photoelectron signals and the residual  $\text{Th}^-$  signals after photodetachment. In this mode, one channel was used to record both signals, since the arrival time of the photoelectrons was much shorter than that of the  $\text{Th}^-$  anions, due to their smaller mass. Since one single laser was used both for the resonant absorption and the photodetachment, it was possible to scan the photon energy from EA/2 to EA. At resonance, a  $\text{Th}^-$  anion could absorb one photon and reach an excited state, after which it could be detached by absorbing a second photon, leading to a signal of the photoelectron. To compensate for the intensity fluctuation of the  $\text{Th}^-$  anion beam, the ratio of the intensity of the photoelectron signal to the intensity of the residual anion beam was monitored as a function of the scanned wavelength, while running the spectrometer at a 20 Hz repetition rate.

### III. RESULTS AND DISCUSSION

To investigate the resonance we used the idle light of an optical parametric oscillator (OPO) laser (primoScan) pumped by 355 nm—the third harmonic of the Nd:YAG (Quanta-Ray Lab 190). The idle light ranges from 700 to 2700 nm with a linewidth of about  $5 \text{ cm}^{-1}$  (150 GHz). The infrared laser is strongly absorbed in some wavelength ranges due to water vapor in the air, leading to a very low signal to noise ratio, so we performed a rough scan ranging from  $4050$  to  $4900 \text{ cm}^{-1}$  (2469–2041 nm) with a step size of  $2 \text{ cm}^{-1}$  (60 GHz) to record a long-range spectrum. As shown in Fig. 2(a), three strong

resonances were observed, labeled T1, T2, and T3. The full widths at half maximum (FWHMs) of the peaks are about  $8 \text{ cm}^{-1}$ , mainly due to the broad linewidth of the OPO laser.

To determine the resonant frequency as accurately as possible, we scanned the observed resonances with a step size of only  $0.2 \text{ cm}^{-1}$  (6 GHz) using the infrared difference frequency generation (DFG) system (Sirah). The infrared laser

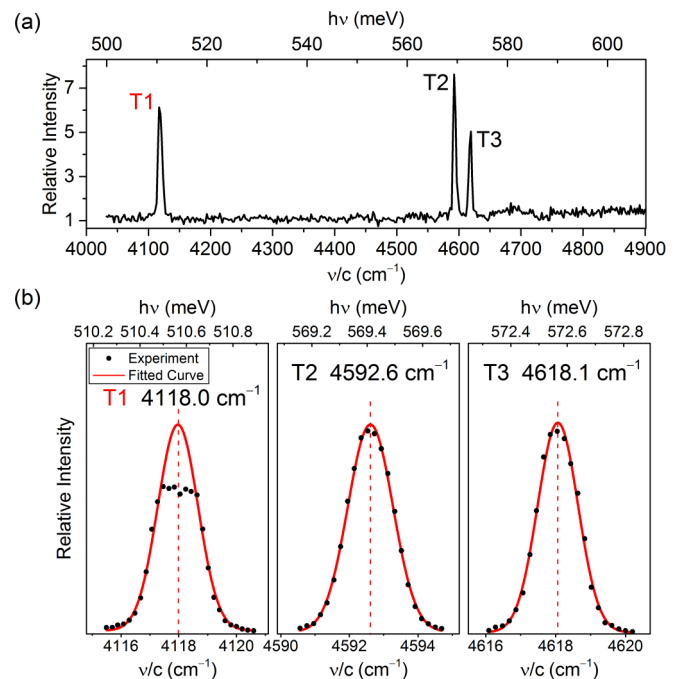


FIG. 2. Survey scan showing three resonances (T1, T2, and T3) in the range from  $4050$  to  $4900 \text{ cm}^{-1}$  (2469–2041 nm) (a) and fine scans of the three resonances T1, T2, and T3 (b). The solid lines indicate Gaussian fits to the experimental data. Peak centers, indicated by the dashed lines, are  $4118.0 \text{ cm}^{-1}$  (2428.4 nm),  $4592.6 \text{ cm}^{-1}$  (2177.4 nm), and  $4618.1 \text{ cm}^{-1}$  (2165.4 nm), respectively. Peak T1 is assigned to the laser-cooling transition  ${}^4F_{3/2}^e \rightarrow {}^2S_{1/2}^o$ .

TABLE I. Excitation energies of Th I.

State	Measured energy		Calculated energy <sup>b</sup>	
	(cm <sup>-1</sup> )	(meV) <sup>a</sup>	(cm <sup>-1</sup> )	(meV) <sup>a</sup>
6d <sup>2</sup> 7s <sup>2</sup> <sup>3</sup> F <sub>2</sub>	0.00	0	0	0
6d <sup>2</sup> 7s <sup>2</sup> <sup>3</sup> P <sub>0</sub>	2558.06	317.159	2684	332.8
6d <sup>2</sup> 7s <sup>2</sup> <sup>3</sup> F <sub>3</sub>	2869.26	355.743	2706	335.5
6d <sup>2</sup> 7s <sup>2</sup> <sup>3</sup> F <sub>2</sub>	3687.99	457.252	3691	457.6
6d <sup>2</sup> 7s <sup>2</sup> <sup>3</sup> P <sub>1</sub>	3865.48	479.258	3788	469.7
6d <sup>2</sup> 7s <sup>2</sup> <sup>3</sup> F <sub>4</sub>	4961.66	615.167	4889	606.2

<sup>a</sup>Reference [55].<sup>b</sup>This work.

was produced by a nonlinear DFG effect between a dye laser and a 1064 nm laser beam which was the residual fundamental output of the pump laser. The dye laser was pumped by 532 nm—the second harmonic output of the Nd:YAG (Quanta-Ray Lab 190). The residual 1064 nm laser was mixed with the dye laser in a nonlinear LiNbO<sub>3</sub> crystal, producing infrared light with a frequency corresponding to the difference between the frequencies of the 1064 nm and the dye laser. The photon energies of the dye laser and the 1064 nm pumping laser were monitored by a wavelength meter (High-Finesse WS6-600) with an uncertainty of 0.02 cm<sup>-1</sup>. The linewidths were 0.06 cm<sup>-1</sup>, and ~1 cm<sup>-1</sup> for the dye laser and the unseeded 1064 nm laser, respectively, leading to ~1 cm<sup>-1</sup> (30 GHz) for the final difference-frequency light. The acquired data of each peak were fitted to a Gaussian function, as shown in Fig. 2(b), where the flat top of the peak T1 was due to the saturation of the resonance absorption. The resonant positions of T1, T2, and T3 were determined to be 4118.0 cm<sup>-1</sup> ( $\lambda = 2428.4$  nm), 4592.6 cm<sup>-1</sup> ( $\lambda = 2177.4$  nm), and 4618.1 cm<sup>-1</sup> ( $\lambda = 2165.4$  nm), respectively, with FWHMs of 1.6 cm<sup>-1</sup> ( $\Delta\nu = 48$  GHz), 1.5 cm<sup>-1</sup> (45 GHz), and 1.4 cm<sup>-1</sup> (42 GHz), correspondingly. The widths of the three peaks mainly come from the DFG laser linewidth of about 1 cm<sup>-1</sup> and the saturation, since other possible contributions (e.g., Doppler broadening, natural linewidth, and power broadening) are significantly smaller. The uncertainty of the resonant position is estimated to be 1.0 cm<sup>-1</sup> (30 GHz).

### A. Transition assignments

We have also extended our calculation for the Th atom to include not only the ground state but also five excited levels, using relativistic configuration interaction (RCI) calculations, based on the wave functions derived from our previous calculations. The comparison with the NIST Atomic Spectra Database (ASD) values shown in Table I reveals good agreement, confirming the reliability of our calculation. To interpret the experimental results, we also extended our calculations to search for all possible bound states of Th anion using the same method. Four more excited states were found in the form of 6d<sup>3</sup>7s<sup>2</sup> <sup>4</sup>P<sub>3/2</sub><sup>e</sup>, 6d<sup>2</sup>7s<sup>2</sup>7p <sup>4</sup>D<sub>3/2</sub><sup>o</sup>, 6d<sup>2</sup>7s<sup>2</sup>7p <sup>4</sup>D<sub>1/2</sub><sup>o</sup>, and 6d<sup>3</sup>7s<sup>2</sup> <sup>4</sup>P<sub>1/2</sub><sup>e</sup>, which are listed along with previous results in Appendix A. Decay branching fractions, transition energies<sup>o</sup>, and transition types of the bound states of anions are key prop-

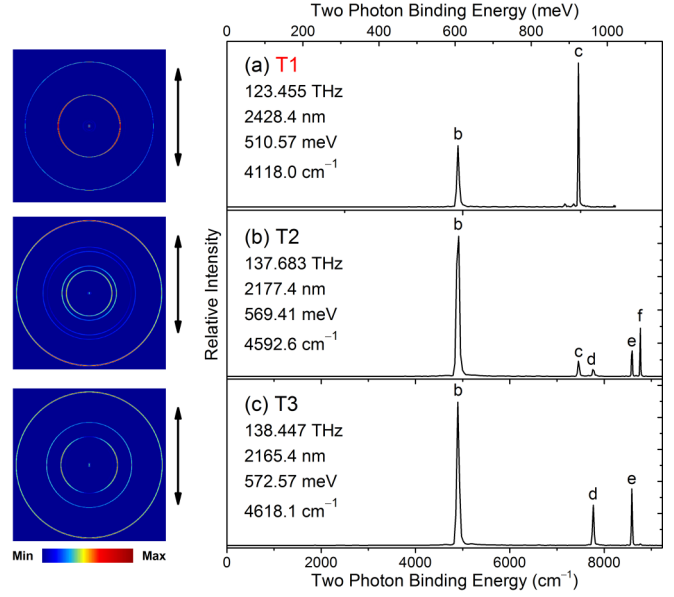


FIG. 3. High-resolution two-photon photoelectron energy spectra and photoelectron images of Th<sup>-</sup> at three observed resonances. The double-headed arrows indicate the laser polarization. The labeling of the peaks corresponds to the ones used in our previous work on one-step detachment experiments [33].

erties for laser cooling and are listed in Table II together with absorption line strengths, which are important since they have a weak dependency on uncertainties in the transition energies. Results are given for levels in the decay paths from <sup>2</sup>S<sub>1/2</sub><sup>o</sup> to <sup>4</sup>F<sub>3/2</sub><sup>e</sup>, including the electric-dipole (E1), electric-quadrupole (E2), magnetic-dipole (M1), and magnetic-quadrupole (M2) transitions. Details for the calculations of all transitions are summarized in Appendix B. From our results, we can deduce that the possible E1-allowed transitions in our scanning range are from the ground state <sup>4</sup>F<sub>3/2</sub><sup>o</sup> to the excited states <sup>2</sup>S<sub>1/2</sub><sup>o</sup>, <sup>4</sup>F<sub>5/2</sub><sup>o</sup>, <sup>4</sup>D<sub>3/2</sub><sup>o</sup>, and <sup>4</sup>D<sub>1/2</sub><sup>o</sup>, where the value for <sup>4</sup>F<sub>3/2</sub><sup>o</sup> ↔ <sup>4</sup>D<sub>3/2</sub><sup>o</sup> (1.98 × 10<sup>-2</sup> a.u.) is one order of magnitude smaller than for the other three transitions, making it unobservable in our experiments due to signal to noise limitation.

To further support the identification of the observed peaks, we analyzed the final states of the photodetachment. In Fig. 3 is shown the photoelectron spectra of the resonant two-photon detachment of Th<sup>-</sup> at the three observed resonant energies. The energy spectra acquired at the three resonances are quite different, where T1 is unambiguously assigned to the laser-cooling transition <sup>4</sup>F<sub>3/2</sub><sup>o</sup> → <sup>2</sup>S<sub>1/2</sub><sup>o</sup> since the observed b (<sup>2</sup>S<sub>1/2</sub><sup>o</sup> → <sup>3</sup>F<sub>2</sub>) and c (<sup>2</sup>S<sub>1/2</sub><sup>o</sup> → <sup>3</sup>P<sub>0</sub>) are strong photodetachment channels according to the selection rules for this process [48]. However, while at the current stage it is not possible to make definite identifications for T2 and T3, a tentative assignment could be <sup>4</sup>F<sub>3/2</sub><sup>e</sup> → <sup>4</sup>F<sub>5/2</sub><sup>o</sup>, and <sup>4</sup>F<sub>3/2</sub><sup>e</sup> → <sup>4</sup>D<sub>1/2</sub><sup>o</sup> for T2 and T3, respectively, pending theoretical confirmation. The assignments of observed peaks are presented in Fig. 4.

### B. Laser cooling of Th anions

Figure 5 illustrates the relevant branchings of the cooling cycle, where we can see that almost 100% of Th<sup>-</sup> in <sup>2</sup>S<sub>1/2</sub><sup>o</sup>

TABLE II. Calculated energy, transition type, lifetimes  $\tau$ , line strengths  $S$ , and branching fractions in the decay paths from  ${}^2S_{1/2}^o$  to  ${}^4F_{3/2}^e$  in  $\text{Th}^-$ . Numbers in parentheses represent powers of 10. A full list can be found in Appendix B.

Upper level	Lower level	Energy (meV)	Type	$\tau^{a,b}$	$S$ (a.u.) <sup>c</sup>	Branching fraction
${}^4G_{5/2}^o$	${}^4F_{3/2}^e$	49.7	E1	51.3 ms	8.98(-1)	1
${}^4F_{5/2}^e$	${}^4F_{3/2}^e$	170.7	M1	0.458 s		0.0460
	${}^4G_{5/2}^o$	121.0	E1		6.63(-3)	0.9540
${}^4F_{7/2}^e$	${}^4F_{3/2}^e$	327.6	E2	8.08 ms		1.16(-7)
	${}^4G_{5/2}^o$	277.8	E1		4.34(-2)	0.9994
	${}^4F_{5/2}^e$	156.8	M1			0.000625
${}^4F_{3/2}^o$	${}^4F_{3/2}^e$	376.0	E1	15.9 $\mu\text{s}$	4.43(0)	0.9968
	${}^4G_{5/2}^o$	326.3	M1			4.10(-8)
	${}^4F_{5/2}^e$	205.3	E1		8.72(-2)	0.003195
	${}^4F_{7/2}^e$	48.5	M2			3.13(-18)
${}^2S_{1/2}^o$	${}^4F_{3/2}^e$	484.0	E1	85.5 $\mu\text{s}$	1.94(-1)	0.99999998
	${}^4G_{5/2}^o$	434.3	E2			1.47(-10)
	${}^4F_{5/2}^e$	313.3	M2			1.80(-13)
	${}^4F_{3/2}^o$	108.0	M1			1.98(-8)

<sup>a</sup>From our previous work [33].

<sup>b</sup>Reference [56].

<sup>c</sup>In atomic units (a.u.); only electric-dipole (E1) transitions were considered.

decays to the ground state directly. A fraction of  $1.47 \times 10^{-10}$  of  $\text{Th}^-$  returns to the ground state through  ${}^4G_{5/2}^o$ , and  $1.98 \times 10^{-8}$  through  ${}^4F_{3/2}^o$ .  ${}^4G_{5/2}^o$  has a long lifetime of 51.3 ms and decaying to this long-lived metastable state could potentially interrupt the fast transition cycle—the  ${}^4G_{5/2}^o$  is a potential dark state from the viewpoint of laser cooling. However, this is fortunate, since the very small branching ratio and the influence of this process are clearly negligible. The period

of laser cooling  $\text{Th}^-$  from 10 K to Doppler temperature  $T_D$  is estimated to be 7.8 s. During the laser-cooling period, only 0.0004% of  $\text{Th}^-$  ends up in  ${}^4G_{5/2}^o$ . The other potential dark state,  ${}^4F_{3/2}^o$ , has a lifetime of only 15.9  $\mu\text{s}$ , so the very few ions that decay to this state will quickly decay back to the ground state. In the absence of an external magnetic field, e.g., in a Paul trap, the fact that  $\text{Th}^-$  does not have hyperfine structures implies that in principle

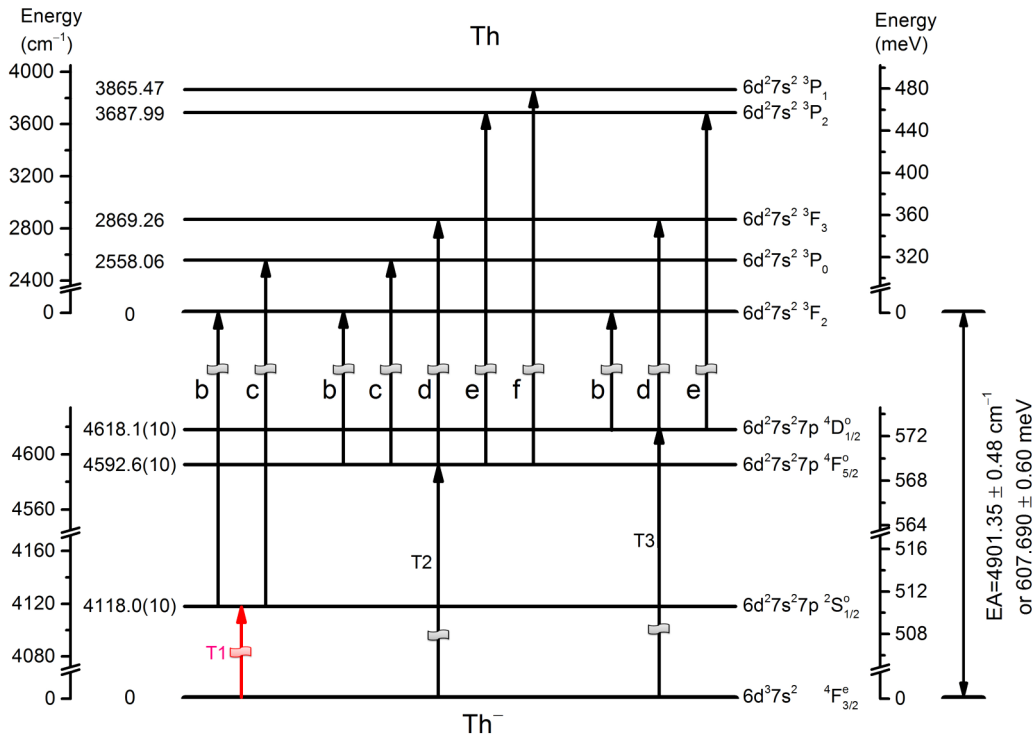


FIG. 4. Partial energy levels of  $\text{Th}^-$  and  $\text{Th}$  related to the observed resonances T1, T2, and T3. The transition labels are the observed peaks in Fig. 3 and are consistent with our previous work [33].

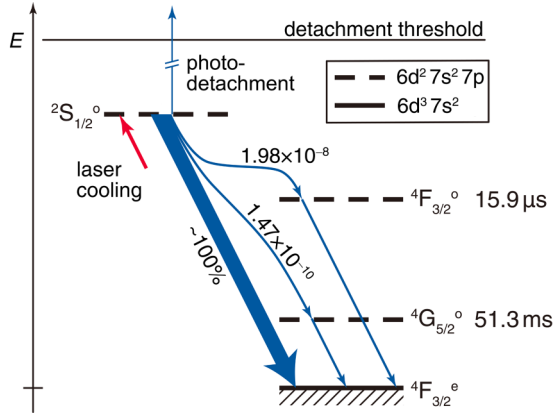


FIG. 5. The decay branches from the  ${}^2S_{1/2}^o$  excited state in  $\text{Th}^-$ . The red arrow indicates the pumping direction for laser cooling. The thicknesses of the blue arrows, which are indicative of branching fractions, and energies are not to scale. The layout of this figure is inspired by Cerchiari *et al.* [31].

only one laser beam [ $\lambda = 2428.4(6)$  nm] is required to realize the laser cooling of  $\text{Th}^-$ . In this case the loss rate due to the photodetachment of the excited  $\text{Th}^-$  during the cooling period is estimated to be 0.025% if using a laser with a narrow linewidth, 1.9 kHz, which is the natural linewidth of the cooling transition (see Appendix C for more discussion).

In a Penning trap, with a magnetic field, the fine structure levels of  $\text{Th}^-$  will split into several  $M_J$  sublevels due to the Zeeman effect, where the splitting is proportional to the magnetic field strength. As an example, in a magnetic field of 1 T, the ground state  ${}^4F_{3/2}^e$  splits up into four sublevels with separations of 6.4 GHz and the excited state  ${}^2S_{1/2}^o$  splits up into two sublevels with a separation of 22.9 GHz. Two laser-cooling schemes (see Fig. 6) are proposed to realize the laser-cooling

in a Penning trap by constructing closed transition cycles. In the first scheme, one cooling laser drives the transition between  ${}^4F_{3/2}^e$   $M_J = -3/2$  and  ${}^2S_{1/2}^o$   $M_J = -1/2$ , and the other three repumping lasers are used to keep the transition cycle closed. In the second scheme, microwave repumping is used instead of laser repumping, and only one laser is required to realize laser cooling.

### C. Sympathetic cooling of antiprotons

If the antiprotons are confined together with the laser-cooled  $\text{Th}^-$  anions in a trap, they can in principle be cooled down to the same temperature as the anions via collisions. To estimate the sympathetic cooling efficiency, a preliminary numerical simulation was conducted using the GPU-accelerated LAMMPS [49] wrapped by the LION package [50]. The antiprotons and  $\text{Th}^-$  anions are cotrapped in a quadrupole Paul trap. A pseudopotential approximation was used in the simulations. One pair of electrodes is held at the ground potential while the amplitude of the rf voltage of the other pair is 2300 V, and its frequency is 20 MHz. The DC voltage on the end caps is  $-4$  V. Characteristic lengths are  $R_0 = 3.5$  mm,  $Z_0 = 10$  mm, and the geometrical factor  $\kappa = 1$  [51,52]. The generated pseudopotential with the rf field is equivalent to a 1.06 T magnetic field in a Penning trap. All pairs of Coulomb interaction are considered. Before simulation starts, all particles are randomly distributed and then thermally equilibrate to 6 K (the typical temperature of buffer cooling).  ${}^{232}\text{Th}^-$  ions are cooled by lasers very quickly and kept at nearly 0 K through the simulation.

Our numerical simulation shows that this is a fast process and the temperature of the antiprotons can be quickly cooled down to a stable minimum of around 2 K. The continued cooling is impeded by the fact that the depth of a Penning trap is inversely proportional to the mass of trapped ions. Therefore, once the Coulomb crystal is formed [46,53,54],  $\text{Th}^-$  anions and antiprotons are separated in space due to

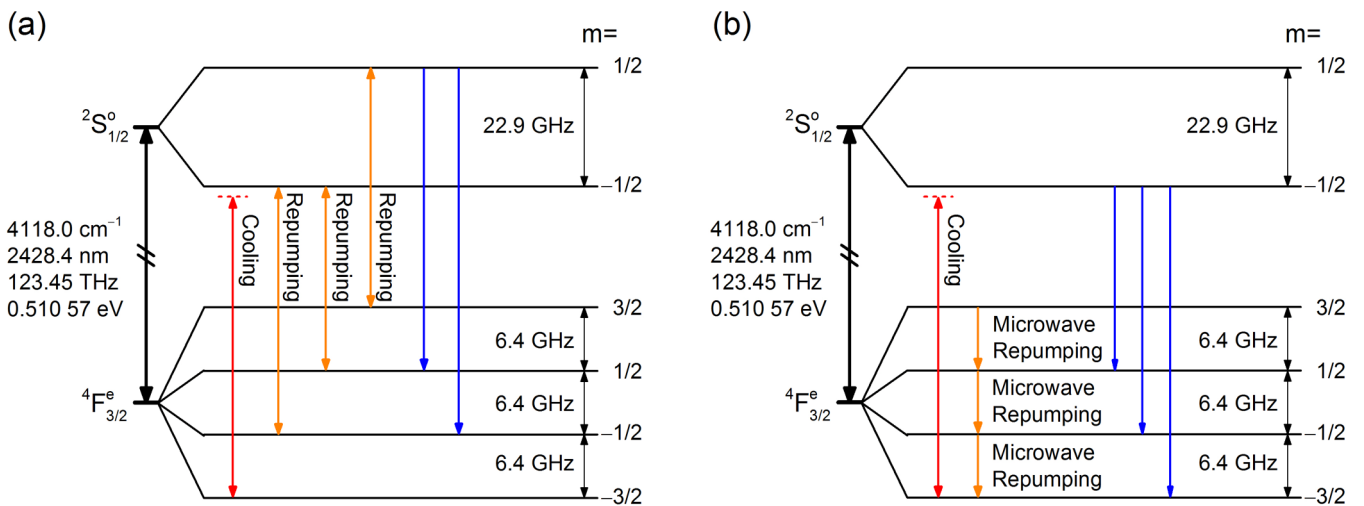


FIG. 6. (a) A cooling scheme using four lasers. A red-tuned cooling laser driving the transition between  ${}^4F_{3/2}^e$   $M_J = -3/2$  and  ${}^2S_{1/2}^o$   $M_J = -1/2$  is used to cool  $\text{Th}^-$  ions. Three repumping lasers are used to keep the transition cycle closed. The two unlabeled arrows indicate two extra spontaneous electric-dipole transitions. (b) A cooling scheme involved microwave repumpings. A red-tuned cooling laser driving the transition between  ${}^4F_{3/2}^e$   $M_J = -3/2$  and  ${}^2S_{1/2}^o$   $M_J = -1/2$  is used to cool  $\text{Th}^-$  ions. A  $\sigma^-$  6.4 GHz ( $\Delta M_J = -1$ ) is used to drive populations on  ${}^4F_{3/2}^e$   $M_J = 3/2, 1/2, -1/2$  to  $M_J = -3/2$ . The three unlabeled arrows indicate three extra spontaneous electric-dipole transitions.

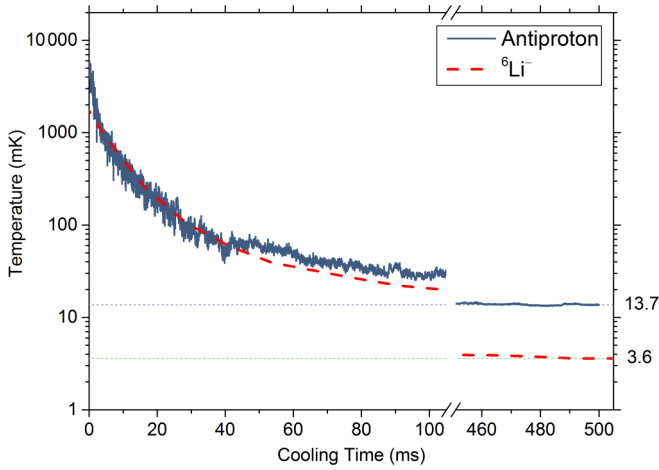


FIG. 7. Simulated results of sympathetic cooling of 300  $^{232}\text{Th}^-$ , 70  $^6\text{Li}^-$ , and ten antiprotons in a Penning trap.  $^{232}\text{Th}^-$  ions are directly laser cooled, while  $^6\text{Li}^-$  and antiprotons lose energies through collisions.

the different depth of the potential well, effectively stopping further collision between  $\text{Th}^-$  ions and antiprotons. To solve this problem, we extended our simulations to add lighter anions  $^6\text{Li}^-$  into the trap as the cooling media. In the simulation, 300 laser-cooled  $\text{Th}^-$  anions, 70  $^6\text{Li}^-$  anions, and ten antiprotons with an initial temperature of 6 K were confined together in the trap. As shown in Fig. 7, the temperature of the antiprotons then continued to quickly decrease from 6 K to 13.7 mK in 500 ms.

#### IV. CONCLUSION

In summary, based on a combination of experimental and theoretical works we have shown that  $\text{Th}^-$  is an excellent candidate for the laser cooling of anions, where the transition

of laser cooling is identified as  $^4F_{3/2}^e \leftrightarrow ^2S_{1/2}^o$ . This cooling cycle is perfectly closed and the fraction of ions ending up in a dark state during the cooling period is only  $4 \times 10^{-6}$ . In sharp contrast to  $\text{La}^-$ , the zero nuclear spin of  $\text{Th}^-$  can significantly reduce the cost of the repumping laser system even if the laser cooling takes place in a magnetic field. This is an important advantage for sympathetically cooling antiprotons because a Penning trap is a more practical choice than a Paul trap to cotrap the anions and antiprotons. Our preliminary ion dynamics simulation showed that the laser-cooled  $\text{Th}^-$  anions can effectively cool antiprotons to a temperature around 10 mK. Before conducting the laser-cooling experiment, an experimental determination of the absolute transition rates, the photodetachment loss, and the resonant frequency of the cooling transition with an accuracy of 1 MHz is required. We will address this question in the near future.

#### ACKNOWLEDGMENTS

This work is supported by the National Natural Science Foundation of China (NSFC) (Grants No. 11974199, No. 21573273, and No. 12074081), the National Key R&D Program of China (Grant No. 2018YFA0306504), and the Strategic Priority Research Program of the Chinese Academy of Sciences (Grant No. XDA02020000). R.S. and T.B. would like to acknowledge support of the Swedish Research Council (VR) under Contract No. 2015-04842. H.L. would like to acknowledge the support of the Hundred Talents Program (CAS).

#### APPENDIX A: MEASURED AND CALCULATED EXCITATION ENERGIES

Measured and calculated excitation energies of  $\text{Th}^-$  states and Zeeman splittings of each state in a 1 T magnetic field are listed in Table III.

TABLE III. Measured and calculated excitation energies of  $\text{Th}^-$  states and Zeeman splittings of each state in a 1 T magnetic field.

State	Measured energy <sup>a</sup>		Calculated energy <sup>a</sup>		$M_J$	Calculated Zeeman splitting (GHz)
	( $\text{cm}^{-1}$ )	(meV)	( $\text{cm}^{-1}$ )	(meV)		
$^4F_{3/2}^e$			0	0.0	-3/2	0.0
					-1/2	6.4
					1/2	12.9
					3/2	19.3
					-5/2	0.0
$^4G_{5/2}^o$			401	49.7	-3/2	10.3
					-1/2	20.6
					1/2	30.9
					3/2	41.2
					5/2	51.5
$^4F_{5/2}^e$	1657(6)	205.4(7)	1377	170.7	-5/2	0.0
					-3/2	14.5
					-1/2	29.0
					1/2	43.5
					3/2	58.0
$^4F_{7/2}^e$	2896(10)	359.1(12)	2642	327.6	5/2	72.4
					-7/2	0.0

TABLE III. (*Continued.*)

State	Measured energy <sup>a</sup>		Calculated energy <sup>a</sup>		$M_J$	Calculated Zeeman splitting (GHz)
	(cm <sup>-1</sup> )	(meV)	(cm <sup>-1</sup> )	(meV)		
${}^4F_{3/2}^o$			3033	376.0	-5/2	17.0
					-3/2	33.9
					-1/2	50.9
					1/2	67.8
					3/2	84.8
					5/2	101.8
					7/2	118.7
${}^4F_{5/2}^e$			3637	451.0	-3/2	0.0
					-1/2	8.4
					1/2	16.9
					3/2	25.3
					-9/2	0.0
					-7/2	17.8
					-5/2	35.6
${}^2S_{1/2}^o$	4118.0(10) <sup>b</sup>	510.57(12) <sup>b</sup>	3904	484.0	-3/2	53.4
					-1/2	71.2
					1/2	89.0
					3/2	106.8
					5/2	124.6
					7/2	142.4
					9/2	160.2
${}^4F_{7/2}^o$			3974	492.7	-1/2	0.0
					1/2	22.9
					-7/2	0.0
					-5/2	14.3
					-3/2	28.5
					-1/2	42.8
					1/2	57.1
${}^4F_{5/2}^o$	4592.6(10) <sup>b</sup>	569.41(12) <sup>b</sup>	3992	495.0	3/2	71.4
					5/2	85.7
					7/2	100.0
					-5/2	0.0
					-3/2	15.1
					-1/2	30.1
					1/2	45.1
${}^4P_{3/2}^e$			4284	531.2	3/2	60.2
					5/2	75.2
					-3/2	0.0
					-1/2	19.5
					1/2	38.9
					3/2	58.4
					-3/2	0.0
${}^4D_{3/2}^o$			4445	551.1	-1/2	15.7
					1/2	31.4
					3/2	47.2
					-1/2	0.0
					1/2	9.7
					3/2	0.0
					1/2	29.7
${}^4D_{1/2}^o$	4618.1(10) <sup>b</sup>	572.57(12) <sup>b</sup>	4503	558.3	-1/2	0.0
					1/2	9.7
					-1/2	0.0
					1/2	9.7
					-1/2	0.0
					1/2	9.7
					1/2	29.7

<sup>a</sup>From our previous work [33], unless otherwise noted.

<sup>b</sup>This work.

#### APPENDIX B: CALCULATED TRANSITION PARAMETERS

Table IV shows predicted transition energies, Einstein coefficients A, line strengths S (E1 transitions only), and branching ratios of all possible decaying transitions.

#### APPENDIX C: PHOTODETACHMENT LOSS RATE

The lifetime of the excited state  ${}^2S_{1/2}^o$  is 85  $\mu$ s. The natural linewidth  $\Delta\nu$  of the transition  ${}^2S_{1/2}^o \leftrightarrow {}^4F_{3/2}^e$  is 1.9 kHz, and the frequency of the transition  $\nu$  is 123.455

TABLE IV. Predicted transition energies, Einstein coefficients  $A$ , line strengths  $S$  (E1 transitions only), and branching ratios of all possible decaying transitions. Four types of transitions are analyzed, electric-dipole (E1), electric-quadrupole (E2), magnetic-dipole (M1), and magnetic-quadrupole (M2), but only the one or two leading terms are listed here. Lifetimes  $\tau$  of each excited state are also calculated. Numbers in parentheses represent powers of 10.

Upper state	Lower state	Transition energy <sup>a</sup>		$\tau^a$ (s)	Type	$S$ (a.u.)	$A$ (s <sup>-1</sup> )	Branching ratio	Total branching ratio	
		cm <sup>-1</sup>	meV							
$^4G_{5/2}^o$	$^4F_{3/2}^e$	401	49.7	5.13(-02)	E1	8.98(-01)	1.95(+01)	1.00(+00)	1.00(+00)	
					M2		2.04(-15)	1.04(-16)		
$^4F_{5/2}^e$	$^4F_{3/2}^e$	1377	170.7	4.58(-01)	M1		1.00(-01)	4.60(-02)	4.60(-02)	
					E2		8.59(-07)	3.93(-07)		
		$^4G_{5/2}^o$	976		121.0	E1	6.63(-03)	2.08(+00)	9.54(-01)	9.54(-01)
			M2		1.27(-11)		5.82(-12)			
$^4F_{7/2}^e$	$^4F_{3/2}^e$	2642	327.6	8.07(-03)	E2		1.44(-05)	1.16(-07)	1.16(-07)	
		$^4G_{5/2}^o$	2241		277.8	E1	4.34(-02)	1.24(+02)	9.99(-01)	9.99(-01)
							M2		1.04(-09)	8.37(-12)
$^4F_{3/2}^o$	$^4F_{5/2}^e$	1265	156.8	E1		7.74(-02)	6.25(-04)	6.25(-04)		
					E2		6.21(-07)	5.01(-09)		
		$^4F_{3/2}^e$	3033		376.0	1.59(-05)	E1	4.43(+00)	6.26(+04)	9.97(-01)
			M2		3.61(-09)		5.76(-14)			
$^4F_{9/2}^e$	$^4G_{5/2}^o$	2632	326.3	E1		2.56(-03)	4.09(-08)	4.10(-08)		
					E2		1.08(-05)	1.72(-10)		
		$^4F_{5/2}^e$	1656		205.3	E1	8.72(-02)	2.01(+02)	3.20(-03)	3.20(-03)
			M2		5.36(-10)		8.53(-15)			
$^4F_{9/2}^e$	$^4F_{7/2}^e$	391	48.5	4.56(+01)	M2		1.96(-13)	3.13(-18)	3.13(-18)	
		$^4G_{5/2}^o$	3237		401.3	M2		9.62(-09)	4.38(-07)	4.38(-07)
							E2		2.39(-06)	1.09(-04)
		$^4F_{5/2}^e$	2260		280.2	E1		2.19(-02)	1.00(+00)	1.00(+00)
$^4F_{7/2}^e$	995		123.4	E2			1.54(-08)	7.02(-07)		
$^2S_{1/2}^o$	$^4F_{3/2}^e$	3904	484.0	8.55(-05)	E1	1.94(-01)	1.17(+04)	1.00(+00)	1.00(+00)	
					M2		5.56(-10)	4.76(-14)		
		$^4G_{5/2}^o$	3503		434.3	E2		1.72(-06)	1.47(-10)	1.47(-10)
							M2		2.10(-09)	1.80(-13)
		$^4F_{3/2}^o$	$^4F_{5/2}^e$		2527	313.3	M1		2.09(-04)	1.79(-08)
$^4F_{3/2}^e$	871			108.0	E2			2.26(-05)	1.93(-09)	
						M2			4.80(-12)	6.61(-16)
$^4F_{7/2}^o$	$^4G_{5/2}^o$	3974	492.7	1.38(-04)	M1		1.09(+00)	1.50(-04)	1.50(-04)	
					E2		3.57(-04)	4.91(-08)		
	$^4F_{5/2}^e$	2597	322.0		E1	1.55(+00)	6.86(+03)	9.44(-01)	9.44(-01)	
						M2		3.59(-10)	4.94(-14)	
	$^4F_{7/2}^e$	$^4F_{3/2}^e$	1332		165.1	E1	6.70(-01)	4.01(+02)	5.52(-02)	5.52(-02)
							M2		1.60(-11)	2.20(-15)
	$^4F_{3/2}^o$	$^4F_{9/2}^e$	941		116.7	E2		2.73(-07)	3.76(-11)	3.76(-11)
$^4F_{9/2}^e$			336	41.7	E1		6.85(-01)	6.60(+00)	9.08(-04)	9.08(-04)
$^4F_{5/2}^o$	$^4F_{3/2}^e$	3992	494.9	4.24(-05)	M2		1.84(-14)	2.53(-18)		
					E1	6.49(-01)	1.40(+04)	5.92(-01)	5.92(-01)	
	$^4G_{5/2}^o$	3592	445.4		M1		3.03(-01)	1.29(-05)	1.29(-05)	
						E2		5.00(-04)	2.12(-08)	
	$^4F_{5/2}^e$	2615	324.2		E1	1.58(+00)	9.57(+03)	4.06(-01)	4.06(-01)	
						M2		3.43(-10)	1.45(-14)	
	$^4F_{7/2}^e$	1350	167.4		E1	7.00(-02)	5.82(+01)	2.47(-03)	2.47(-03)	
						M2		1.55(-11)	6.57(-16)	
	$^4F_{3/2}^o$	959	118.9		M1		1.15(-02)	4.89(-07)	4.89(-07)	
						E2		7.02(-08)	2.97(-12)	
$^4F_{9/2}^e$	$^2S_{1/2}^o$	355	44.0	E2		9.62(-09)	4.08(-13)	4.08(-13)		
		$^2S_{1/2}^o$	89		11.0	E2		5.42(-14)	2.30(-18)	2.30(-18)
$^4F_{7/2}^o$	$^4F_{7/2}^e$	19	2.4	M1		7.97(-08)	3.38(-12)	3.38(-12)		
					E2		4.77(-17)	2.02(-21)		

TABLE IV. (*Continued.*)

Upper state	Lower state	Transition energy <sup>a</sup>		$T^a$ (s)	Type	$S$ (a.u.)	$A$ (s <sup>-1</sup> )	Branching ratio	Total branching ratio	
		cm <sup>-1</sup>	meV							
$^4P_{3/2}^e$	$^4F_{3/2}^e$	4284	531.1	2.74(-04)	M1		1.84(-01)	5.05(-05)	5.09(-05)	
		E2			1.30(-03)		3.57(-07)			
	$^4G_{5/2}^o$	3884	481.6		E1		9.89(-02)	2.94(+03)	8.04(-01)	8.04(-01)
		M2						6.17(-16)	1.69(-19)	
	$^4F_{5/2}^e$	2908	360.5		M1			7.64(-02)	2.09(-05)	2.10(-05)
		E2						3.03(-04)	8.30(-08)	
	$^4F_{7/2}^e$	1642	203.6		M2			2.49(-05)	6.81(-09)	6.81(-09)
		$^4F_{3/2}^o$	1252		155.2		E1	7.02(-01)	6.97(+02)	1.91(-01)
	M2							5.05(-11)	1.38(-14)	
	$^2S_{1/2}^o$	381	47.2		E1		2.76(-01)	7.73(+00)	2.12(-03)	2.12(-03)
M2					1.56(-14)	4.28(-18)				
$^4F_{7/2}^o$	311	38.6	M2		1.19(-16)	3.27(-20)	3.27(-20)			
	$^4F_{5/2}^o$	292	36.2	E1	1.39(-01)	1.18(+01)	3.24(-03)	3.24(-03)		
M2					6.17(-16)	1.69(-19)				
$^4D_{3/2}^o$	$^4F_{3/2}^e$	4445	551.1	1.80(-04)	E1	1.98(-02)	8.81(+02)	1.59(-01)	1.59(-01)	
		M2			2.06(-11)		3.71(-15)			
	$^4G_{5/2}^o$	4044	501.4		M1			1.30(-01)	2.34(-05)	2.34(-05)
		E2						4.26(-05)	7.68(-09)	
	$^4F_{5/2}^e$	3068	380.4		E1		3.19(-01)	4.67(+03)	8.41(-01)	8.41(-01)
		M2						2.41(-10)	4.34(-14)	
	$^4F_{7/2}^e$	1803	223.5		M2			2.93(-10)	5.29(-14)	5.29(-14)
		$^4F_{3/2}^o$	1412		175.1		M1		5.97(-06)	1.07(-09)
	E2							4.81(-07)	8.66(-11)	
	$^2S_{1/2}^o$	541	67.1		M1			2.67(-04)	4.80(-08)	4.80(-08)
E2					2.09(-10)	3.76(-14)				
$^4F_{7/2}^o$	471	58.4	E2		1.11(-09)	2.00(-13)	2.00(-13)			
	$^4F_{5/2}^o$	452	56.0	M1		7.28(-04)	1.31(-07)	1.31(-07)		
E2					1.30(-09)	2.34(-13)				
$^4P_{3/2}^e$	160	19.8	E1	1.27(-01)	2.65(-01)	4.78(-05)	4.78(-05)			
	M2				7.58(-17)	1.37(-20)				
$^4D_{1/2}^o$	$^4F_{3/2}^e$	4503	558.3	4.44(-05)	E1	2.43(-01)	2.25(+04)	1.00(+00)	1.00(+00)	
		M2			7.63(-10)		3.39(-14)			
	$^4G_{5/2}^o$	4102	508.6		E2			5.66(-05)	2.51(-09)	2.51(-09)
		$^4F_{5/2}^e$	3126		387.6		M2		3.42(-09)	1.52(-13)
	$^4F_{3/2}^o$		1470		182.3		M1		1.34(-03)	5.93(-08)
		E2						1.57(-07)	6.99(-12)	
	$^2S_{1/2}^o$	599	74.3		M1			4.17(-03)	1.85(-07)	1.85(-07)
		$^4F_{5/2}^o$	510		63.2		E2		1.56(-09)	6.95(-14)
	$^4P_{3/2}^e$		218		27.0		E1	6.72(-02)	7.10(-01)	3.15(-05)
		M2						5.60(-16)	2.49(-20)	
$^4D_{3/2}^o$	58	7.2	M1		7.77(-06)	3.45(-10)	3.45(-10)			
	E2				4.32(-14)	1.92(-18)				
$^4P_{1/2}^e$	$^4F_{3/2}^e$	4940	612.5	3.45(-04)	M1		1.51(-02)	5.22(-06)	7.79(-06)	
		E2			7.44(-03)		2.56(-06)			
	$^4G_{5/2}^o$	4540	562.8		M2			4.47(-09)	1.54(-12)	1.54(-12)
		$^4F_{3/2}^o$	1907		236.5		E1	4.06(-01)	2.85(+03)	9.83(-01)
	$^2S_{1/2}^o$		1037		128.5		E1	2.11(-02)	2.39(+01)	8.23(-03)
		$^4D_{3/2}^o$	495		61.4		E1	1.98(-01)	2.44(+01)	8.41(-03)
	$^4D_{1/2}^o$		437		54.2		E1	1.69(-02)	1.43(+00)	4.93(-04)

<sup>a</sup>From our previous work [33] except last four excited states.

THz. The light intensity in a saturated absorption is given by

$$I = \frac{8\pi h\nu^3}{g_2 c^2} \Delta\nu = 3.3 \times 10^{-8} \text{ W/cm}^2,$$

where  $g_2 = 2$  is the degeneracy number of the excited state,  $g_1 = 4$  for the ground state,  $h$  is the Planck constant, and  $c$  is the light speed.

The theoretical photodetachment cross section  $\sigma$  of  $^2S_{1/2}^o$  at  $\nu = 123.455$  THz is  $4.8 \times 10^{-20} \text{ m}^2$ . The photoelectron

number  $n_{\text{electron}}$  in the laser-cooling period ( $t = 7.8$  s) is given by

$$n_{\text{electron}} = \frac{ItN_2\sigma}{h\nu} = 1.26 \times 10^{-3}N_2,$$

where  $N_2$  is the number of atoms at the excited state. Therefore the photodetachment loss rate

$$\frac{\Delta N}{N} = \frac{n_e}{N_1 + N_2} = \frac{1}{5} \times 1.26 \times 10^{-3} = 0.252 \times 10^{-3}.$$

This photodetachment loss rate 0.025% is negligible. Note: for the saturated absorption, we have

$$\frac{N_2}{N_1} = \frac{g_2}{2g_1} = \frac{1}{4}.$$

The cost of a laser with a narrow linewidth  $\Delta\nu = 1.9$  kHz is pretty high. If a laser with a wider linewidth is used, for example,  $\Delta\nu = 190$  kHz, the photodetachment loss rate is 2.5% in a saturated absorption. It is still acceptable.

- [1] T. K. Langin, G. M. Gorman, and T. C. Killian, *Science* **363**, 61 (2019).
- [2] D. S. Jin and J. Ye, *Chem. Rev.* **112**, 4801 (2012).
- [3] M. Amoretti, C. Amsler, G. Bonomi, A. Bouchta, P. Bowe, C. Carraro, C. L. Cesar, M. Charlton, M. Collier, M. Doser, V. Filippini, K. S. Fine, A. Fontana, M. C. Fujiwara, R. Funakoshi, P. Genova, J. S. Hangst, R. S. Hayano, M. H. Holzschneider, L. V. Jorgensen *et al.*, *Nature* **419**, 456 (2002).
- [4] M. Ahmadi, B. X. R. Alves, C. J. Baker, W. Bertsche, E. Butler, A. Capra, C. Carruth, C. L. Cesar, M. Charlton, S. Cohen, R. Collister, S. Eriksson, A. Evans, N. Evetts, J. Fajans, T. Friesen, M. C. Fujiwara, D. R. Gill, A. Gutierrez, J. S. Hangst *et al.*, *Nature* **541**, 506 (2016).
- [5] S. Gerber, J. Fesel, M. Doser, and D. Comparat, *New J. Phys.* **20**, 023024 (2018).
- [6] A. Kellerbauer, M. Amoretti, A. S. Belov, G. Bonomi, I. Boscolo, R. S. Brusa, M. Büchner, V. M. Byakov, L. Cabaret, C. Canali, C. Carraro, F. Castelli, S. Cialdi, M. de Combarieu, D. Comparat, G. Consolati, N. Djourellov, M. Doser, G. Drobychev, A. Dupasquier *et al.*, *Nucl. Instrum. Methods Phys. Res., Sect. B* **266**, 351 (2008).
- [7] M. Ahmadi, B. X. R. Alves, C. J. Baker, W. Bertsche, E. Butler, A. Capra, C. Carruth, C. L. Cesar, M. Charlton, S. Cohen, R. Collister, S. Eriksson, A. Evans, N. Evetts, J. Fajans, T. Friesen, M. C. Fujiwara, D. R. Gill, A. Gutierrez, J. S. Hangst *et al.*, *Nat Commun.* **8**, 681 (2017).
- [8] M. Doser *et al.* (AEgIS Collaboration), *Classical Quantum Gravity* **29**, 184009 (2012).
- [9] A. Kellerbauer and J. Walz, *New J. Phys.* **8**, 45 (2006).
- [10] G. Gabrielse, X. Fei, L. A. Orozco, R. L. Tjoelker, J. Haas, H. Kalinowsky, T. A. Trainor, and W. Kells, *Phys. Rev. Lett.* **63**, 1360 (1989).
- [11] G. Gabrielse, W. S. Kolthammer, R. McConnell, P. Richerme, R. Kalra, E. Novitski, D. Grzonka, W. Oelert, T. Sefzick, M. Zielinski, D. Fitzakerley, M. C. George, E. A. Hessels, C. H. Storry, M. Weel, A. Müllers, and J. Walz (ATRAP Collaboration), *Phys. Rev. Lett.* **106**, 073002 (2011).
- [12] G. B. Andresen *et al.* (ALPHA Collaboration), *Phys. Rev. Lett.* **105**, 013003 (2010).
- [13] N. Madsen, F. Robicheaux, and S. Jonsell, *New J. Phys.* **16**, 063046 (2014).
- [14] N. Kuroda, H. A. Torii, K. Yoshiki Franzen, Z. Wang, S. Yoneda, M. Inoue, M. Hori, B. Juhász, D. Horváth, H. Higaki, A. Mohri, J. Eades, K. Komaki, and Y. Yamazaki, *Phys. Rev. Lett.* **94**, 023401 (2005).
- [15] G. Gabrielse, N. S. Bowden, P. Oxley, A. Speck, C. H. Storry, J. N. Tan, M. Wessels, D. Grzonka, W. Oelert, G. Schepers, T. Sefzick, J. Walz, H. Pittner, T. W. Hänsch, and E. A. Hessels (ATRAP Collaboration), *Phys. Rev. Lett.* **89**, 233401 (2002).
- [16] M. Ahmadi, B. X. R. Alves, C. J. Baker, W. Bertsche, E. Butler, A. Capra, C. Carruth, C. L. Cesar, M. Charlton, S. Cohen, R. Collister, S. Eriksson, A. Evans, N. Evetts, J. Fajans, T. Friesen, M. C. Fujiwara, D. R. Gill, A. Gutierrez, J. S. Hangst *et al.*, *Nature* **548**, 66 (2017).
- [17] M. Ahmadi, B. X. R. Alves, C. J. Baker, W. Bertsche, A. Capra, C. Carruth, C. L. Cesar, M. Charlton, S. Cohen, R. Collister, S. Eriksson, A. Evans, N. Evetts, J. Fajans, T. Friesen, M. C. Fujiwara, D. R. Gill, J. S. Hangst, W. N. Hardy, M. E. Hayden *et al.*, *Nature* **557**, 71 (2018).
- [18] ALPHA Collaboration, *Nature* **578**, 375 (2020).
- [19] M. Bohman, A. Mooser, G. Schneider, N. Schön, M. Wiesinger, J. Harrington, T. Higuchi, H. Nagahama, C. Smorra, S. Sellner, K. Blaum, Y. Matsuda, W. Quint, J. Walz, and S. Ulmer, *J. Mod. Opt.* **65**, 568 (2018).
- [20] M. Doser (AEgIS Collaboration), *J. Phys.: Conf. Ser.* **199**, 012009 (2010).
- [21] T. Andersen, *Phys. Rep.* **394**, 157 (2004).
- [22] T. Andersen, H. K. Haugen, and H. Hotop, *J. Phys. Chem. Ref. Data* **28**, 1511 (1999).
- [23] L. Pan and D. R. Beck, *Phys. Rev. A* **82**, 014501 (2010).
- [24] R. C. Bilodeau and H. K. Haugen, *Phys. Rev. Lett.* **85**, 534 (2000).
- [25] U. Warring, M. Amoretti, C. Canali, A. Fischer, R. Heyne, J. O. Meier, C. Morhard, and A. Kellerbauer, *Phys. Rev. Lett.* **102**, 043001 (2009).
- [26] A. Fischer, C. Canali, U. Warring, A. Kellerbauer, and S. Fritzsche, *Phys. Rev. Lett.* **104**, 073004 (2010).
- [27] C. W. Walter, N. D. Gibson, C. M. Janczak, K. A. Starr, A. P. Snedden, R. L. Field, and P. Andersson, *Phys. Rev. A* **76**, 052702 (2007).
- [28] C. W. Walter, N. D. Gibson, Y. G. Li, D. J. Matyas, R. M. Alton, S. E. Lou, R. L. Field, D. Hanstorp, L. Pan, and D. R. Beck, *Phys. Rev. A* **84**, 032514 (2011).
- [29] C. W. Walter, N. D. Gibson, D. J. Matyas, C. Crocker, K. A. Dungan, B. R. Matola, and J. Rohlen, *Phys. Rev. Lett.* **113**, 063001 (2014).
- [30] E. Jordan, G. Cerchiari, S. Fritzsche, and A. Kellerbauer, *Phys. Rev. Lett.* **115**, 113001 (2015).
- [31] G. Cerchiari, A. Kellerbauer, M. S. Safronova, U. I. Safronova, and P. Yzombard, *Phys. Rev. Lett.* **120**, 133205 (2018).
- [32] P. Yzombard, M. Hamamda, S. Gerber, M. Doser, and D. Comparat, *Phys. Rev. Lett.* **114**, 213001 (2015).
- [33] R. L. Tang, R. Si, Z. Fei, X. X. Fu, Y. Lu, T. Brage, H. Liu, C. Chen, and C. G. Ning, *Phys. Rev. Lett.* **123**, 203002 (2019).

- [34] A. Osterwalder, M. J. Nee, J. Zhou, and D. M. Neumark, *J. Chem. Phys.* **121**, 6317 (2004).
- [35] C. Hock, J. B. Kim, M. L. Weichman, T. I. Yacovitch, and D. M. Neumark, *J. Chem. Phys.* **137**, 244201 (2012).
- [36] X. B. Wang and L. S. Wang, *Rev. Sci. Instrum.* **79**, 073108 (2008).
- [37] R. L. Tang, X. X. Fu, and C. G. Ning, *J. Chem. Phys.* **149**, 134304 (2018).
- [38] X. X. Fu, J. M. Li, Z. H. Luo, X. L. Chen, and C. G. Ning, *J. Chem. Phys.* **147**, 064306 (2017).
- [39] X. L. Chen and C. G. Ning, *J. Chem. Phys.* **145**, 084303 (2016).
- [40] Z. Luo, X. Chen, J. Li, and C. Ning, *Phys. Rev. A* **93**, 020501(R) (2016).
- [41] X. L. Chen and C. G. Ning, *J. Phys. Chem. Lett.* **8**, 2735 (2017).
- [42] R. L. Tang, X. L. Chen, X. X. Fu, H. Wang, and C. G. Ning, *Phys. Rev. A* **98**, 020501(R) (2018).
- [43] Y. Lu, R. L. Tang, X. X. Fu, and C. G. Ning, *Phys. Rev. A* **99**, 062507 (2019).
- [44] W. C. Wiley and I. H. McLaren, *Rev. Sci. Instrum.* **26**, 1150 (1955).
- [45] I. León, Z. Yang, H. T. Liu, and L. S. Wang, *Rev. Sci. Instrum.* **85**, 083106 (2014).
- [46] A. T. J. B. Eppink and D. H. Parker, *Rev. Sci. Instrum.* **68**, 3477 (1997).
- [47] B. Dick, *Phys. Chem. Chem. Phys.* **16**, 570 (2014).
- [48] P. C. Engelking and W. C. Lineberger, *Phys. Rev. A* **19**, 149 (1979).
- [49] S. Plimpton, *J. Comput. Phys.* **117**, 1 (1995).
- [50] E. Bentine, C. J. Foot, and D. Trypogeorgos, *Comput. Phys. Commun.* **253**, 107187 (2020).
- [51] D. J. Berkeland, J. D. Miller, J. C. Bergquist, W. M. Itano, and D. J. Wineland, *J. Appl. Phys.* **83**, 5025 (1998).
- [52] S. Willitsch, M. T. Bell, A. D. Gingell, and T. P. Softley, *Phys. Chem. Chem. Phys.* **10**, 7200 (2008).
- [53] D. J. Wineland, J. C. Bergquist, W. M. Itano, J. J. Bollinger, and C. H. Manney, *Phys. Rev. Lett.* **59**, 2935 (1987).
- [54] F. Diedrich, E. Peik, J. M. Chen, W. Quint, and H. Walther, *Phys. Rev. Lett.* **59**, 2931 (1987).
- [55] E. Tiesinga, P. J. Mohr, D. B. Newell, and B. N. Taylor, The 2018 CODATA Internationally Recommended Values of the Fundamental Physical Constants (Web Version 8.0). Database developed by J. Baker, M. Douma, and S. Kotochigova (National Institute of Standards and Technology, Gaithersburg, MD, 2019). Available at <http://physics.nist.gov/constants>.
- [56] F. A. Babushkin, *Acta Phys. Pol.* **25**, 749 (1964).